

Solid-State Colloidal CuInS₂ Quantum Dot Solar Cells enabled by Bulk Heterojunctions

D. So^a, S. Pradhan^a and G. Konstantatos^{a,b,†}

Received 00th January 20xx,
Accepted 00th January 20xx

DOI: 10.1039/x0xx00000x

www.rsc.org/

Colloidal copper indium sulfide (CIS) nanocrystals (NCs) are Pb- and Cd-free alternatives for use as absorbers in quantum dot solar cells. In a heterojunction with TiO₂, non-annealed ligand-exchanged CIS NCs form solar cells yielding a meager power conversion efficiency (PCE) of 0.15%, with photocurrents plummeting far below predicted values from absorption. Decreasing the amount of zinc during post-treatment leads to improved mobility but marginally improves device performance (PCE = 0.30%). By incorporating CIS into a porous TiO₂ network, we saw an overall drastic improvement in device performance, reaching PCEs of 1.16%, mainly from an increase in short circuit current density (J_{sc}) and fill factor (FF) and a 10-fold increase in internal quantum efficiency (IQE). We have determined that by moving from a bilayer to a bulk heterojunction architecture, we have reduced the trap-assisted recombination as seen in changes in the ideality factor, the intensity dependence of the photocurrent and transient photocurrent (TPC) and photovoltage (TPV) characteristics.

Introduction

As a low-cost and adaptive technology, colloidal quantum dot solar cells, mostly based on PbS, have reached impressive PCEs in a little over a decade from proof of concept devices (PCE ~ 0.01%) in 2005¹ to more than 10% in 2016². Most of these developments have come from an understanding of the material properties as well as the device operation and the experimental solutions that address or improve on them³, such as enhancing carrier mobilities^{4,5}, tuning band edges^{6,7}, controlling the surface passivation^{8,9}, designing the device architecture^{10–17}, choosing appropriate ohmic contacts¹⁸ and doping active layers^{19–22} among others. This technology however contains Pb and can raise concerns on its regulatory acceptance.

Devices made from bulk copper indium gallium diselenide (CIGS), while containing a thin toxic cadmium-containing buffer layer, have exhibited one of the most competitive efficiencies, achieving 21.0%²³. Although this value is encouraging, solar cells from colloidal-synthesized nanocrystalline CIGS, in particular

its derivative copper indium sulfide (CIS), have PCEs below 10%. These NCs are usually annealed^{24–26} and/or placed in contact with CdS^{27–31}, which negate both the cost-effectiveness and adaptability provided by the colloidal nanocrystal platform, and also the low toxicity of the elements in CIS nanocrystals. For those which have not been sintered or used CdS as a buffer layer, CIS NCs have been employed as sensitizers in liquid junction solar cells^{32–34} with a highest efficiency of 7%³³ reaching 11.6% for its selenide analogue³⁵. In this architecture however, CIS is not used as an absorber film that facilitates charge transport and the presence of a liquid electrolyte is required.

For CIS NCs to be employed in the same manner as PbS in quantum dot, solid-state solar cells, a film deposition technique that does not require annealing and results in photoconductive films is needed. Recently, we have reported a ligand-exchange strategy with formic acid to form photoconductive CIS films³⁶. A device architecture which does not utilize CdS, then, has to be developed. Bulk CIS, crystallized from precursor inks, has been shown to form a heterojunction with TiO₂^{37–39}. While for CIS NCs, with mild annealing, Schottky²⁶ and ZnO^{24,25} heterojunction solar cells have been reported but with modest photocurrents and efficiencies. In this work, we report solar cells made from CIS NCs and nanocrystalline TiO₂. We improve on film mobilities, vary device architecture and identify the material properties limiting device performance. Finally we propose a mechanism for the device operation. By the end of this work, we have improved the efficiency of non-annealed ligand-exchanged CIS NC-based devices from 0.2% to 1.2%.

Experimental

^a ICFO, Institute of Photonic Sciences, The Barcelona Institute of Science and Technology, Castelldefels 08860, Spain

^b Institució Catalana de Recerca i Estudis Avançats (ICREA), Passeig Lluís Companys 23, 08010 Barcelona, Spain

† gerasimos.konstantatos@icfo.es

Electronic Supplementary Information (ESI) available: UPS spectra, series and shunt resistances, error values, Mott-schottky calculations, absorption coefficient, effects of reduced Zn, additional SEM images, transient photocurrent and transient photovoltage curves and other equations used for Urbach energy calculation. See DOI: 10.1039/x0xx00000x

Chemicals and stock solutions

Ethylcellulose: 46 cP (5 % in 80:20 toluene/ethanol), formic acid 98%, oxalic acid 99%, glutaric acid 99%, pimelic acid 98%, titanium tetrachloride (TiCl₄) 99%, titanium isopropoxide 97%, bis(trifluoromethane)sulfonimide lithium salt (LiTFSI) 99.95%, anhydrous chlorobenzene 99.8% and 4-tert-butylpyridine (TBP) 96% were purchased Sigma-Aldrich Co., LLC; 90T titania paste from Dyesol Ltd.; concentrated hydrochloric acid (HCl), isopropanol, ethanol, methanol, acetonitrile and toluene from Panreac Quimica SLU; spiro-MeO-TAD livilux™ SHT-263 from Merck & Co. Inc. All chemicals were used without further purification.

Various stock solutions were prepared beforehand and are described as follows. 1M TiCl₄ stock solution: deionized water (125 mL) and concentrated HCl (20.85 mL) were placed in a flask in an ice bath. Under stirring, TiCl₄ (27.5 mL) was added dropwise. The solution was stirred until it was clear and stored and kept below 0°C until future use. TiO₂ blocking layer: a weakly acidic solution of titanium isopropoxide was prepared by mixing titanium isopropoxide (369 µL) into isopropanol (2.53 mL). To this, isopropoxide (2.53mL) with 2M aqueous HCl (35 µL) was added dropwise. This solution was used fresh. F52C stock solution (90T and ethylcellulose): equal volumes of diluted 90T paste (1:1.25wt 90T with ethanol) and 10%wt ethylcellulose in ethanol were combined and vortexed. Spiro-MeO-TAD solutions: spiro-OMeTAD (45 mg/mL) in chlorobenzene was prepared. This (800 µL) was combined with a dopant solution containing 85mg/mL LiTFSI (15 µL) in acetonitrile and TBP (10 µL).

Synthesis of thiol-free CIS nanocrystals

Thiol-free CIS nanocrystals were synthesized according to our previous work³⁶. Briefly, copper and indium halides were dissolved in oleylamine, trioctylphosphine and octadecene. At a target temperature, bis(trimethylsilyl) sulfide was injected to form the chalcogenide. After this, the product was isolated and overcoated with a modified treatment of corresponding amounts of zinc oleate at 80°C: 1.0 Zn, 0.6585g zinc acetate dihydrate; 0.3 Zn, 0.2195g (third) and 0.1 Zn, 0.0658g (tenth). The amount of nanocrystal, oleic acid and octadecene during post-treatment were kept the same. The final product was washed and dispersed in toluene.

Porous and dense TiO₂ electrodes

Densely packed TiO₂ nanocrystalline electrodes were fabricated by spincoating a diluted solution of 90T paste (1:2.5 wt. 90T with ethanol) on cleaned, masked 12mm x 12mm FTO-coated glass (Pilkington TEC 15, Xop Glass) at 3000RPM using a Specialty Coating Systems 6800 series spin-coater system for 30 seconds. These films were then annealed in air starting at 100°C with 100°C increments, holding for 15 minutes at each increment. At 500°C, the film was annealed for an hour at that temperature and then allowed to cool naturally. To improve the connectivity between the TiO₂ nanocrystals, the annealed films were immersed for 20 minutes in a 70°C bath of 40mM TiCl₄, prepared by aqueous dilution from a 1M TiCl₄ stock solution.

The films were then dried and annealed using the previously described annealing profile.

Porous TiO₂ nanocrystalline electrodes were fabricated by first spincoating (3000RPM, 30s) on cleaned FTO-coated glass a weakly acidic solution of titanium isopropoxide which was then annealed using the previous annealing profile to deposit a dense 50nm-TiO₂ blocking layer. On top of this blocking layer, a combined solution (F52C) of diluted 90T paste and an ethanolic solution of ethylcellulose was spincoated (3000RPM, 30s) and annealed. This paste (F52C) was diluted accordingly to control the thickness of the porous layer, with a 50% dilution in ethanol leading to a thickness of 500nm. A densification step was performed to improve the connectivity between the TiO₂ nanocrystals; the annealed films were immersed for 20 minutes in a 50°C bath of 10mM TiCl₄, prepared by aqueous dilution from a 1M TiCl₄ stock solution. The films were then rinsed, dried and annealed.

Device Fabrication

TiO₂ films were flushed with methanol and toluene before the deposition of CIS. A solution of 25mg/mL CIS in toluene was allowed to settle on the surface of the TiO₂ electrode for 30s, and afterwards was spun at 2000RPM for 30s. Whilst spinning, a drop of 2%vol formic acid in methanol was reacted on the film and finally was rinsed with methanol and toluene. This cycle constitutes one layer of the layer-by-layer (LbL) deposition process. Multiple layers were deposited, starting from 6 layers up until 18 layers. Optionally, spiro-OMeTAD solutions were spincoated (2000RPM, 30s) on top of the final layer as a way of preventing shorts. All devices were fabricated in air. Top electrodes of 75nm Au and 100nm Ag were consecutively thermally evaporated (Kurt J Lesker Nano 36) through masks with 2mm diameter holes.

Materials Characterization

The Fermi level and band edge positions of ligand-exchanged films and of annealed TiO₂ were determined using ultra-violet photoelectron spectroscopy (SPECS PHOIBOS 150 electron spectrometer Hel, 21.2 eV. ICN2, Spain). Photoluminescence transients of TiO₂ and adsorbed CIS nanocrystals were measured (Horiba FL1057) using a 636nm laser excitation. The TiO₂ film was immersed in a 1M methanol solution of the diacids for 2 days and rinsed with methanol before the adsorption of CIS. Different thicknesses, determined by sample cross section (scanning electron microscopy, FEI SEM FEG Inspect) of CIS were deposited on FTO and the absorption (Cary 5000 UV-Vis-NIR spectrophotometer) was taken to get the absorption coefficient.

The composition of CIS with varying treatments of zinc was analysed by energy dispersive x-ray spectroscopy (FEI SEM FEG Inspect INCA). To measure the carrier mobilities with varying Zn content, field effect transistors (FETs) were fabricated as before³⁶, by depositing 30nm of the material via the LbL process onto 285 nm thermally-grown silica on p-doped silicon whereby top contacts with 1 mm channel widths and 30 µm channel lengths were thermally deposited through masks. Mobility and

majority carrier type of the NC solid were determined from the transfer characteristics (Agilent B1500A) of the FETs.

The changes in film porosity were analyzed through Brunauer-Emmett-Teller adsorption (TriStar 3000, CCIT-UB). Large quantities of densified TiO₂ substrates based on 90T and its modification were fabricated and carefully scraped to form a powder. Samples were heated to 450°C for at least 3 hours prior to the measurement to remove adsorbed moisture. The pore size distribution was obtained by performing Barrett-Joyner-Halenda analyses on the adsorption isotherm.

Device Characterization

The current voltage characteristics of completed devices in the dark and under simulated sunlight (100 mW cm⁻² AM1.5G, Oriel Sol3A) were recorded using a Keithley 2400 sourcemeter controlled by in-house developed LabView programs. The spectrally-resolved external quantum efficiency was obtained by measuring the short circuit current of devices illuminated with monochromatic light (Newport Oriel apex) of known intensity (Newport 818-UV photodiode). Capacitance-voltage profiling of solar cells was performed on an Agilent B1500A semiconductor parameter analyser.

To determine the extent of CIS infiltration into TiO₂, the depth profile of devices without contacts was analyzed using time-of-flight secondary ion mass spectrometry (Ion TOF IV, IBEC, Spain) under positive polarity, probing key elements in each layer (CIS, In; TiO₂, Ti; SnO₂:F, Sn; SiO₂, Si).

Transient photovoltage (TPV) and photocurrent (TPC) of the devices were measured with an in-house-built set-up, comprised of a xenon arc lamp, a 637-nm laser (Vortran Stradus) and an Agilent 4000X oscilloscope. The white lamp provided for the steady open circuit voltage (V_{oc}) of the device, whose intensity was controlled by an external applied voltage and was attenuated with a metal-mesh when needed. The laser with a frequency of 10 Hz and pulse width of 500 μ s was controlled by a function generator; its intensity was controlled to keep the voltage transient amplitude not more than 5% of the steady state light bias. The oscilloscope recorded the data using a 1 M Ω input impedance for the TPV measurement and a 50 Ω input for the TPC measurement. In the same set-up, the intensity-dependent V_{oc} and J_{sc} were measured with a Xenon arc lamp calibrated with Newport 818-UV power meter and an Agilent 4000X oscilloscope. The accuracy of this measurement was estimated to be within $\pm 8\%$. All electrical characterization of the devices was performed in air.

The photoluminescence of ligand-exchanged films and those in contact with TiO₂ is small. We measured the emission of ligand-exchanged CIS of various layers on different TiO₂ substrates by micro-Raman spectroscopy (Renishaw InVia), exciting the sample with a 785nm laser and probing the high Raman shift regions which corresponded to the luminescence range of the material.

Results and Discussion

CIS-TiO₂ Bilayer devices

CIS NCs have band edges which match well with that of TiO₂, allowing for the formation of a type II heterojunction (Fig. 1a). Through ultraviolet photoelectron spectroscopy, these band edges were obtained by locating the Fermi level from the cut-off energy of biased samples, and the valence band edge by adding the value of the onset of unbiased samples to the Fermi level. (Fig. S1). The band edges and Fermi level position of the smallest bandgap material agree with that reported by Borchert²⁶. We see that for CIS of different sizes, the Fermi level remains fixed. This has been seen in other materials as an indication of high trap or defect density⁴⁰. With changes in size, the valence band edge also remains roughly constant, with shifts being more apparent in conduction band edge positions. This has similarity with that of PbX and CdX (X=S, Se or Te)⁴¹. Because of the favorable band edge positions of TiO₂ and CIS, we see that the photoluminescence lifetime (excited at 636 nm, probed at 770 nm) systematically decreases with decreasing CIS-TiO₂ distance (Fig. 1b), which has been observed for thinner ZnS shells⁴². This indicates that charge transfer occurs from CIS NCs to TiO₂.

Indeed, when layers of CIS are deposited onto TiO₂, a heterojunction with a built-in potential of almost 0.6 V forms. Annealed CIS nanocrystals in contact with various materials have led to solar cells with various open circuit voltages (V_{oc}): CdS, V_{oc} 0.48-0.71 V²⁹⁻³¹; ZnO, V_{oc} 0.40-0.46 V^{24,25}; P3HT or PSiF-DBT, V_{oc} \sim 0.25-0.54 V^{43,44}; with bulk CIS on TiO₂³⁷⁻³⁹ giving a similar V_{oc} of 0.49-0.57 V. We placed CIS QDs on TiO₂ via a ligand exchange layer-by-layer (LbL) process, without any post-processing annealing and then deposited Au via thermal evaporation, as shown in the inset of Fig. 1c. Completed devices show a near constant capacitance for low applied voltages (Fig. 1c) indicating that they are nearly depleted, which through Mott-Schottky analysis (Fig. S2) yields depletion widths of 125 nm, close to the absorber thickness (170 nm). In agreement with the previously reported carrier concentration for this material³⁶, we calculated a carrier concentration of 2×10^{16} cm⁻³: a moderate value given the marked off-stoichiometry of the material^{36,45}. The device performance is shown in Table 1 and Table S1. For the material synthesized at 170°C, the performance is near identical to that reported for a CIS NC-ZnO bilayer heterojunction²⁴. The series resistance of solar cells made from smaller particles increases, most likely due to their lower mobility³⁶. The spectral response of the external quantum efficiency (EQE) of the solar cells follows the absorption of the CIS QDs and can be tuned with size (Figure 1d). The V_{oc} , however, in line with the determined constant Fermi level positions, does not increase with size.

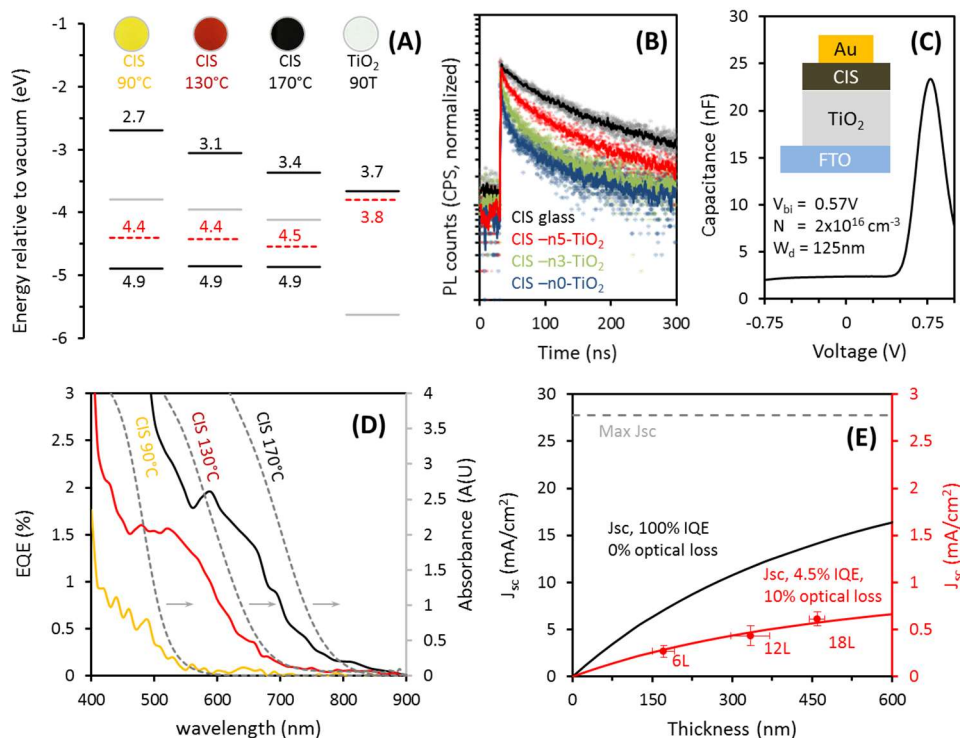


Fig. 1 CIS NCs have favorable band edges with respect to TiO₂ but result in devices with low J_{sc} . (a) Conduction band edges obtained from UPS, showing a type II heterojunction with TiO₂ and a near constant Fermi level for different NC sizes. (b) Transient photoluminescence of dilute CIS-130°C solution deposited on TiO₂ with various adsorbed diacids: n0, oxalic acid; n3, glutaric acid; n5, pimelic acid. (c) The capacitance-voltage profile of a CIS-TiO₂ bilayer device showing a flat profile at low applied voltages, with the inset depicting the device structure. (d) EQE spectra of CIS-TiO₂ bilayer devices corresponding well with the absorption spectra of the respective nanocrystals. (e) Thickness-dependent predicted J_{sc} (black) using obtained extinction coefficient values (CIS 170°C). The J_{sc} (400nm bandpass-filtered) of solar cells of various NC absorber thicknesses (red), fitted with a predicted J_{sc} for devices with 4.5% IQE and 10% optical loss.

Table 1. Device performance of various sizes of CIS, thicknesses and Zn content on flat-TiO₂ (90T).

CIS	Zn	layers	V_{oc}	J_{sc}	FF	PCE
90°C	1.0	6	0.50	0.011	0.29	0.002
130°C	1.0	6	0.55	0.077	0.25	0.011
170°C	1.0	6	0.59	0.91	0.27	0.15
170°C	1.0	12	0.60	0.93	0.32	0.19
170°C	1.0	18	0.61	1.08	0.33	0.22
170°C	0.3	6	0.63	1.26	0.31	0.23
170°C	0.3	12	0.62	1.39	0.30	0.29
170°C	0.3	18	0.60	1.67	0.33	0.33
170°C	0.1	6	0.63	1.81	0.26	0.30

Despite the relatively high V_{oc} , these devices have J_{sc} s far from their maximum expected values. The absorption coefficient (Fig. S3) was obtained by measuring the transmission and reflection of three films of known thicknesses with values comparable to previous reports²⁴ yet much lower than that of bulk CIS⁴⁶. By assuming an internal quantum efficiency of unity and no optical losses, a predicted J_{sc} was calculated by taking the double-pass total absorbed AM 1.5G light as the total current, leading to a maximum J_{sc} of 27.8 mA/cm² (Fig. 1e), with a predicted 14.9 mA/cm² for a film of 500 nm. Clearly, the results from Table 1 indicate that the values we obtained are far from the predicted values. The J_{sc} barely changes with

increasing layer thickness, as, for thinner films, more of the back reflected light reaches the front TiO₂. However, when incoming light is filtered (400 nm) to exclude UV light, we see the J_{sc} increases with increasing thickness (Fig. 1e). These data points can be fitted with a J_{sc} prediction, by assuming an internal quantum efficiency (IQE) of 4.5% and 10% optical loss. This signifies poor charge collection and transport in the absorber film.

Effects of reduced Zn content

We aimed at improving charge transport in the CIS film by reducing Zn during the post-treatment overcoating. For these nanocrystals, during post-treatment with Zn-oleate, it has been proposed³⁶ that zinc incorporates itself through the surface, by adsorption and by replacement of indium which is rich on the surface. This zinc-rich shell could hinder transport in the NC film. We reduced the amount of zinc from its usual amount, to a third and to a tenth of this content, maintaining all other amounts the same. In Table S2, we see a reduction in zinc corresponding with our modifications. As well, indium increases with decreasing zinc while copper and sulfur remain comparatively the same. The lower amount of zinc leads to a lower PL quantum yield but leads to a more red-shifted emission (Fig. S4). For assembled solids with native ligands, we see that for the same shift from the photoluminescence peak λ_p , at $\lambda_p + 50$ nm, the PL decay is faster for nanocrystals with lower Zn content, showing

improved coupling between nanocrystals in the ensemble. Correspondingly, for ligand-exchanged films this results in improved mobility (Fig. S5). We see that J_{sc} increases with decreasing Zn (Table 1) and that when UV light is excluded (400 nm filter) from the incident light, the J_{sc} can be fitted well with an absorption-predicted J_{sc} , assuming an IQE of 6.5% and 10% optical loss: an improvement from the fitted IQE of 4.5% (Fig. S5). The total J_{sc} can be increased to twice its value from 1.0 Zn to 0.1 Zn; unfortunately, going lower than this Zn value lessens the colloidal stability³⁶ of the material. While reducing Zn enhances J_{sc} , IQE remains low and fill factors (FFs) are less than 50%. PbS with a comparable mobility and at a particular adjusted absorption leads to a much higher J_{sc} ⁴⁷ and suggests that in this material, mobility is not the only deterrent for good device performance.

CIS-TiO₂ bulk heterojunction devices

For materials with poor electrical properties, most works have turned to using a blended architecture to boost photovoltaic performance. The famous example of this is in the field of organic solar cells⁴⁸, wherein excitons need an interface to split them into free charges. For inorganic nanocrystalline solar cells, largely based on PbS, the formation of a blend or interpenetrated architecture allows for improved charge extraction when one material is prone to electrical loss¹⁵, for passivation of traps by compensating charges¹⁶ and for overcoming short diffusion lengths^{13,14,17}. For CIS, in the bulk, improvements in the current and/or fill factor were achieved by incorporating it in porous TiO₂³⁷, in ZnO nanowires⁴⁹ and in a PbS NC solid⁵⁰. These structures use CIS as electron donors; similarly copper indium chalcogenide nanocrystals have been used as electron acceptors in a blend with polymers such as P3HT^{51,52} and PCPDTBT⁵³. For QD-sensitized solar cells, this blended architecture is implicitly attained but bypasses charge transport in the absorber.

We are able to form a blended structure using nanocrystalline TiO₂ and colloiddally-synthesized CIS NCs by increasing the pore diameter of TiO₂. We engineered the porosity of the TiO₂ layer by adding ethylcellulose as a soft sacrificial template to the 90T paste. Ethylcellulose also acts to increase viscosity so, for a particular modification, despite having half the TiO₂ content, the resulting film thickness remains the same as that of the unmodified paste. The Barrett-Joyner-Halenda (BJH) transformation of the Brunauer-Emmett-Teller (BET) adsorption isotherm indicates the formation of large volumes of bigger pore species with the addition of ethylcellulose (Fig. 2a). The pore-size distribution also shows that the features from nanocrystalline TiO₂ interstices and the mesopores from the native porogen are preserved. These new larger pores allow for the infiltration of CIS. Cross-sectional images of completed devices reveal that for the unmodified 90T paste, a thick NC absorber rests on top of an assembly of particles whereas for 90T with added ethylcellulose, no thick absorber layer forms and an assembly of particles with more rounded features is seen (Fig. 2b). CIS NCs deposited on FTO and on 90T show no thickness difference with various numbers of

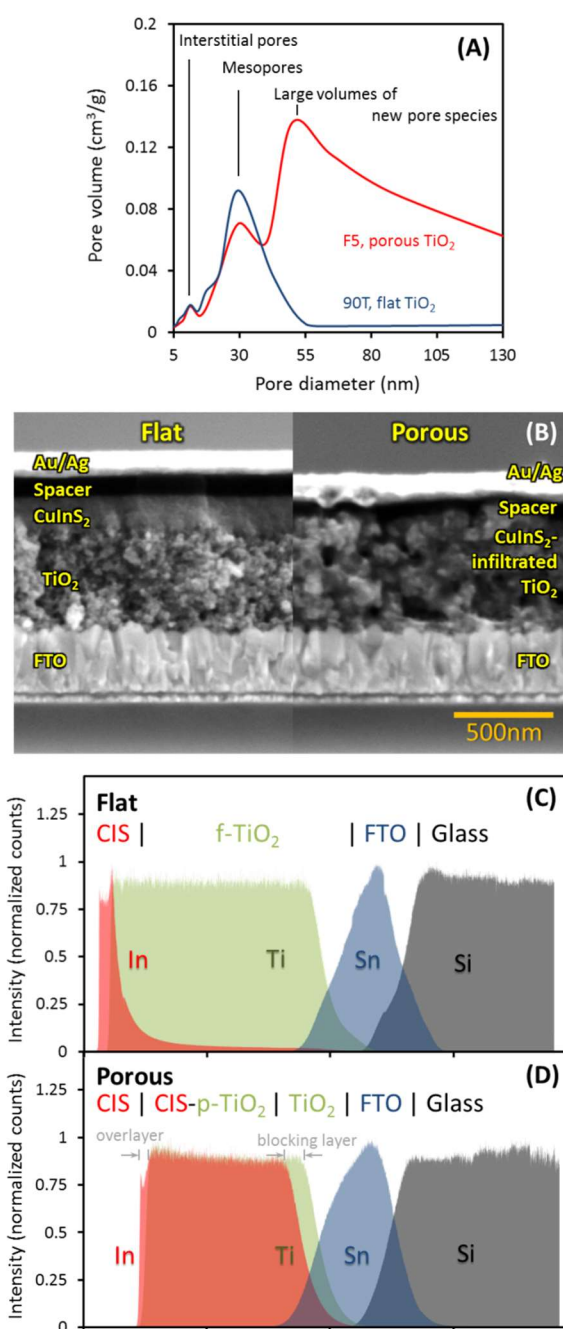


Fig. 2 Increasing the porosity of TiO₂ allows for the infiltration of CIS QDs. (a) Pore diameter distribution (BJH transformation of BET curves) showing large volumes of new pore species. (b) Cross-sectional SEM images of a CIS on flat-TiO₂ device (left) and a CIS-infiltrated porous TiO₂ device (right). (c and d) Secondary ion mass spectra of flat (c) and porous (d) devices, probing key elements in each layer to demonstrate deep infiltration in porous devices.

deposited layers and this signifies that no infiltration takes place in the 90T substrates (Fig. S6). This absence of infiltration is further confirmed by depth analysis of key elements (Fig. 2c, 2d, Fig. S7) via secondary ion mass spectrometry (SIMS). No infiltration occurs for CIS on 90T while for CIS on porous TiO₂, the infiltration is uniform and reaches the rear of the porous film, showing the presence of the deposited blocking layer and the formation of an overlayer.

Table 2. Device performance of CIS with different Zn content on various TiO₂ substrates (f-TiO₂, flat TiO₂; p-xxx, porous TiO₂ xxx nm thick).

Zn	layers	TiO ₂	V _{oc}	J _{sc}	FF	PCE
1.0	6	f-TiO ₂	0.59	0.91	0.27	0.15
1.0	6	p-500	0.60	2.18	0.50	0.65
0.3	6	f-TiO ₂	0.63	1.26	0.31	0.23
0.3	6	p-500	0.65	2.66	0.52	0.87
0.3	12	p-850	0.67	3.83	0.39	1.01
0.3	12	p-850	0.70	4.32	0.38	1.16a
0.1	6	f-TiO ₂	0.63	1.81	0.26	0.30
0.1	6	p-500	0.67	1.82	0.36	0.44

^achampion device

This infiltrated structure leads to improved solar cell performance. Devices with CIS in porous TiO₂, that is BHJ devices, have improved IV characteristics (Fig. 3a) showing an improved FF, J_{sc}, V_{oc} and no cross-over in the dark and light curves. This crossover in the IV has been attributed to high charge barriers in CIGS devices⁵⁴. For different contents of zinc and different thicknesses, BHJ devices demonstrate statistically higher currents, leading to more than double the total current (Table 2, S3), where the contribution from CIS is increased more than 5 times (Fig. S8). The differences in the fill factor are also clearly demarcated, with an average of around 30% for bilayer

improved charge collection from the CIS absorber layer over bilayer devices as seen in the EQE and IQE (Fig. 3d,e, albeit having differences from the observed J_{sc}), given their comparable full device light absorption (Fig. S9). We note that spiro-MeO-TAD acts as a spacer and that whilst devices without it function as well (Fig. S10); it has been put in place to reduce shorting particularly in porous devices. The thickness of the blended material can be modified by increasing the thickness of the TiO₂ network (Fig. S11) through controlled dilution of the F52C paste (methods section). Thicker films however are prone to cracking and delamination. For a thickness of 850nm, the infiltration of CIS into TiO₂ is confirmed by SIMS (Fig. S7). We see that the short circuit current density increases with the thickness of this blended material (Fig. 3f) for CIS with 1.0 Zn and 0.3 Zn. For 0.1 Zn however, while it displays a much higher J_{sc} in a bilayer device, it does not benefit from TiO₂ porosity, displaying an invariant J_{sc} with porous TiO₂ thickness. From cross-sectional SEM (Fig. S12), we see that CIS 1.0 Zn and CIS 0.3 Zn infiltrate the TiO₂ network comparably, with similar overlayer thicknesses, and that CIS 0.1 Zn does not infiltrate the porous network: rather it just builds up on its surface. These confirm that not only the porosity of TiO₂ but that the infiltration of CIS in the network results in better device performance.

The improved performance of the blended architecture of CIS-infiltrated TiO₂ is caused by reduced trap-assisted recombination. We see different behaviors in the intensity

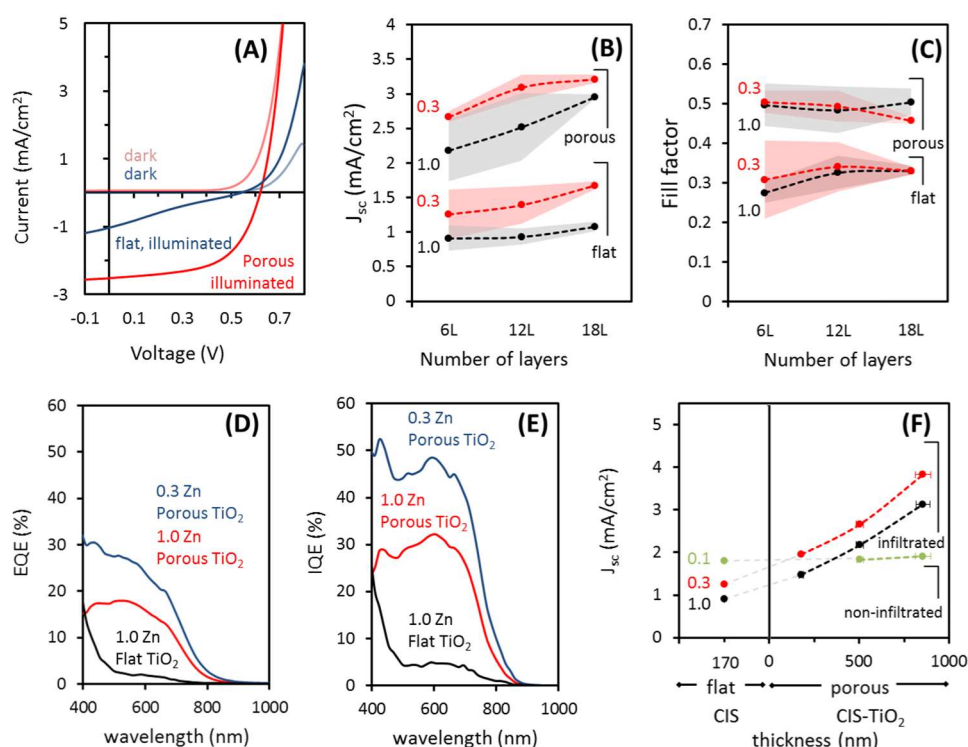


Fig. 3 Infiltration of CIS into TiO₂ drastically improves performance. (a) Dark and illuminated IV curves of CIS on flat bilayer (blue) and porous TiO₂ BHJ (red) devices. (b) J_{sc} and (c) FF of devices with different numbers of deposited CIS layers (6L, 12L, 18L), Zn content (1.0, 0.3 Zn) and types of titania (flat, porous), error bars shown as shaded regions. (d) EQE and (e) IQE spectra of devices based on 1.0 Zn CIS on flat TiO₂ (black), 1.0 Zn CIS on 500nm-porous TiO₂ (red) and 0.3 Zn CIS on 500nm-porous TiO₂ (blue). (f) J_{sc} of devices from CIS of various Zn content on flat TiO₂ and infiltrated into porous TiO₂ of different TiO₂ thicknesses.

devices and 50% for BHJ ones. BHJ devices demonstrate dependence (suns) of the V_{oc} (Fig. 4a) and the J_{sc} (Fig. 4b) of

bilayer and BHJ devices. The Suns- V_{oc} curve (Fig. 4a) can give a value of the light ideality factor n_{id} , with n_{id} close to unity indicating band to band recombination is dominant and $n_{id} > 1$ indicating trap-assisted recombination. Two regimes appear in both bilayer and BHJ devices: low intensity conditions and conditions close to 1 sun. In both these regimes, the BHJ device demonstrates near-invariant n_{id} 's (low, 1.0; high, 1.5) much closer to 1 than those of bilayer devices which show poorer n_{id} at low light intensity (low, 3.8; high, 2.1). This large deviation from unity points to trap-assisted recombination being dominant in bilayer devices. Furthermore, the suns- J_{sc} (Fig. 4b), fitted with a power law, can also be used to gain insight into the device operation, with the power law exponent α close to 1 being a mark of ideal generation-limited solar cells, 0.75 for space-charge-limited recombination and 0.5 for trap assisted recombination routes⁵⁵. Again, we see that two regimes appear, one for low light and another for close to 1 sun conditions and that for BHJ devices, there is little difference in these regimes. BHJ devices give a close to ideal $\alpha = 0.89$, while bilayer devices yield $\alpha = 0.62$, agreeing with the suns- V_{oc} finding that bilayer devices suffer from trap-assisted recombination.

Transient photocurrent (Fig. S13a) and photovoltage measurements (Fig. S13b) further support these claims. The transient photovoltage (Fig. S13b) of bilayer devices shows a bi-exponential decay, having a short lifetime from 0-10 ms and an extremely long one from 25 ms onwards. This extremely long exponential decay, whose contribution to the transient photovoltage lessens with decreasing light intensity, we attribute to trapped carriers which maintain the quasi-Fermi level difference for a much longer time. In BHJ devices, having a longer lifetime in the 0-10 ms range, the transient photovoltage is single exponential for all light intensities. This longer photovoltage decay coupled with the longer photocurrent decay of BHJ devices (Fig. S13a) leads to the observed improved current density. From the TPC and TPV curves, it is possible to calculate the carrier lifetime, recombination rate, excess charge carrier density generated by the laser pulse and the Urbach energy (supporting information). For a given excess charge carrier density, the carrier lifetime in BHJ devices is higher, which consequently leads to a much lower recombination rate (Fig. 4c, d). From Fig. 4d, the slope in the double-log plot predicts the recombination order of the device, the first order pertaining to trap-assisted recombination; the second, radiative recombination and the third, Auger recombination. Consistent with the results presented thus far, we see a shift from a device performance experiencing loss from trap-assisted recombination in flat devices to a more ideal solar cell seen in BHJ devices.

These traps can be treated as a density of tail states in the CIS energy gap that shifts in the presence of TiO_2 . Before collection or transport, when photogenerated charges relax into these states, an activation energy E_U or the Urbach energy is needed to be overcome to bring them to an energy E_t that would allow for transport. Likewise it is the mean energy of the exponential distribution of available states beyond the band edges. We have calculated the Urbach energy (Fig. 5a) by fitting the tail region of the EQE^{56,57}. As well, alternative estimations of

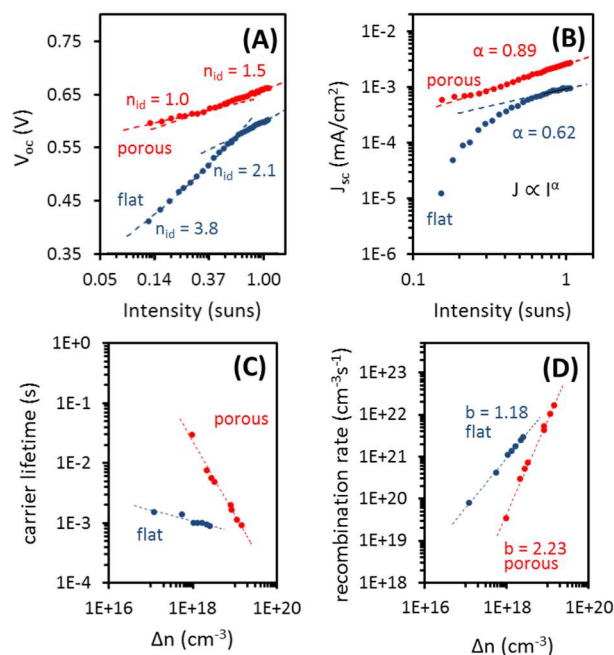


Fig. 4 The improved performance is due to reduced trap-assisted recombination and lower Urbach energy. (a) Suns- V_{oc} and (b) suns- J_{sc} showing enhancement in ideality factor and a power law dependence closer to unity. (c) Carrier lifetime and (d) recombination rate vs excess charge carrier density of bilayer and BHJ devices giving two clearly different slopes which relate to their recombination order.

the Urbach energy can be obtained from the carrier lifetime and excess carrier density against voltage⁵⁸ (Fig. S12). We see that the bilayer devices require a much higher activation energy (~ 160 meV) to remove charges from these tail states than in BHJ devices (80 meV). Accounting for discrepancies in the E_U values through different methods⁵⁹, the trend is similar using other E_U estimations (Fig. S13, Table S4)—that the BHJ devices show lower E_U than flat ones. This difference in E_U is supported by the photoluminescence of these devices. We performed micro-Raman-photoluminescence to look into the emission of thin layers (~ 25 nm) of CIS deposited on flat and porous TiO_2 (Fig. 5b). When the CIS layer is thin, the emission peaks at 847 nm in both flat and porous devices. However, when slightly thicker CIS (~ 75 nm) is deposited, flat devices have a redshifted peak at 886 nm, whereas the photoluminescence peak of porous devices remains unchanged. This PL shift corresponds to a 64 meV difference and agrees well with the difference in Urbach energy.

We suspect that TiO_2 provides non-photogenerated electrons to quench holes which enter the deep tail states in CIS. Shabaev et. al. calculated from theoretical models that hole levels near the degenerate valence band contribute to long absorption tails⁶⁰. This model however implies that the unique photoluminescence of CIS is inherent to its band structure and not due to defect states. There is still no clear consensus on the PL mechanism in CIS⁶¹: as donor-acceptor emission, as quantum-confined conduction band to acceptor level transition, as donor level to quantum-confined valence band transition, or as an inherent property due to the band structure. We believe though that the nanocrystals emit through a

transition between quantum-confined conduction band to acceptor level, considering the extent to which the emission can be tuned³⁶ and that the conduction band minimum shifts to a greater extent than the valence band maximum with changes in size (Fig. 1a). Further, in completed CIS devices, Halpert, et. al. suggested that deep trapping of holes³⁰ could be responsible for low fill factors. In support of this, it was suggested that upon the photogeneration of carriers, holes become delocalized through self-trapping⁶². Whether it be due to inherent long tails or dense trap levels forming a distribution, we find it reasonable to place these tail/dense states near the valence band (Fig. 5c). Because of poor transport and a built-in field that resists the injection of electrons into CIS, TiO₂ can only provide electrons for a finite thickness which is at least 25 nm into the CIS film (Fig. 5b). In BHJ devices where the pore size is around 50 nm (Fig. 2a), CIS will be easily accessed by TiO₂ for injection. These injected electrons quench holes in the deeper tail states. In turn, this shifts the distribution of occupied tail states much closer to the valence band, would lower the activation energy needed to remove carriers from these states and would shift the photoluminescence to higher energies (Fig. 5b). That is to say that in these devices, the mechanism is not through exciton splitting as there is an increase in photocurrent with thickness (Fig. 1e, S5) and that there is no decrease in photoluminescence in blended devices (Fig. S14).

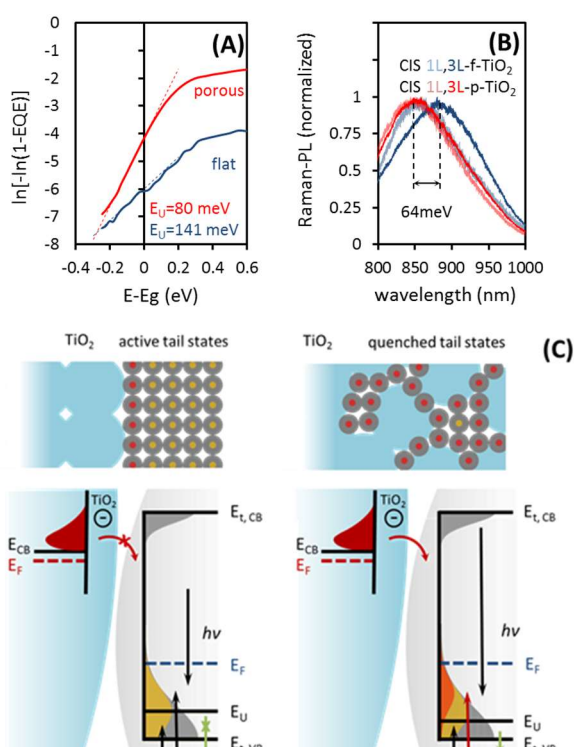


Fig. 5 Trapped carriers and lower activation energy for extraction in BHJ devices. Lower Urbach energy (a) seen for BHJ devices and results in a more blue shifted emission (b). TiO₂ filling tail states in CIS more effectively in BHJ devices (c).

Conclusions

Copper indium sulfide is a promising nontoxic quantum-confined nanocrystal material that has not been fully explored as an absorber in quantum dot solar cells. We have fabricated non-annealed heterojunction solar cells of colloiddally synthesized CIS nanocrystals with nanocrystalline TiO₂ and found that their performance was far from what can be predicted through absorption even when improving mobility. We turned to using a porous TiO₂ network as the anode and saw a dramatic increase in photocurrents and fill factors, with an almost six-fold increase in efficiency reaching 1.2%. We have identified that these devices have less trap-assisted recombination and suggested that BHJ devices allow for better quenching of deeper tail states in CIS by TiO₂. This work opens up CIS as a viable material for non-annealed quantum dot solar cells, highlighting important material properties and device operations that need to be considered. Further work lies in increasing the absorber blend thickness and mobility.

Acknowledgements

The research leading to these results has received funding from Fundació Privada Cellex, and European Community's Seventh Framework program (FP7-ENERGY.2012.10.2.1) under grant agreement 308997. We also acknowledge financial support from the Spanish Ministry of Economy and Competitiveness (MINECO) and the "Fondo Europeo de Desarrollo Regional" (FEDER) through grant MAT2014-56210-R. This work was also supported by AGAUR under the SGR grant (2014SGR1548). G.K. acknowledges financial support from the Spanish Ministry of Economy and Competitiveness, through the "Severo Ochoa" Programme for Centres of Excellence in R&D (SEV-2015-0522).

References

- 1 S. a McDonald, G. Konstantatos, S. Zhang, P. W. Cyr, E. J. D. Klem, L. Levina and E. H. Sargent, *Nat. Mater.*, 2005, **4**, 138–142.
- 2 M. Yuan, M. Liu and E. H. Sargent, *Nat. Energy*, 2016, **1**, 16016.
- 3 G. H. Carey, A. L. Abdelhady, Z. Ning, S. M. Thon, O. M. Bakr and E. H. Sargent, *Chem. Rev.*, 2015, **115**, 12732–12763.
- 4 Y. Liu, M. Gibbs, J. Puthussery, S. Gaik, R. Ihly, H. W. Hillhouse and M. Law, *Nano Lett.*, 2010, **10**, 1960–1969.
- 5 J. Zhang, J. Tolentino, E. R. Smith, J. Zhang, M. C. Beard, A. J. Nozik, M. Law and J. C. Johnson, *J. Phys. Chem. C*, 2014, **118**, 16228–16235.
- 6 P. R. Brown, D. Kim, R. R. Lunt, N. Zhao, M. G. Bawendi, J. C. Grossman and V. Bulović, *ACS Nano*, 2014, **8**, 5863–5872.
- 7 C.-H. M. Chuang, P. R. Brown, V. Bulović and M. G. Bawendi, *Nat. Mater.*, 2014, **13**, 1–6.
- 8 A. H. Ip, S. M. Thon, S. Hoogland, O. Voznyy, D. Zhitomirsky, R. Debnath, L. Levina, L. R. Rollny, G. H. Carey, A. Fischer, K. W. Kemp, I. J. Kramer, Z. Ning, A. J. Labelle, K. W. Chou, A. Amassian and E. H. Sargent, *Nat. Nanotechnol.*, 2012, **7**, 577–582.
- 9 Y. Cao, A. Stavrinadis, T. Lasanta, D. So and G. Konstantatos, *Nat. Energy*, 2016, **1**, 16035.
- 10 C. Piliago, L. Protesescu, S. Z. Bisri, M. V. Kovalenko and M. A. Loi, *Energy Environ. Sci.*, 2013, **6**, 3054.
- 11 A. G. Pattantyus-Abraham, I. J. Kramer, A. R. Barkhouse, X. Wang, G. Konstantatos, R. Debnath, L. Levina, I. Raabe, M. K.

- Nazeeruddin, M. Grätzel and E. H. Sargent, *ACS Nano*, 2010, **4**, 3374–3380.
- 12 S. M. Willis, C. Cheng, H. E. Assender and A. A. R. Watt, *Nano Lett.*, 2012, **12**, 1522–1526.
- 13 J. Jean, S. Chang, P. R. Brown, J. J. Cheng, P. H. Rekemeyer, M. G. Bawendi, S. Gradečak and V. Bulović, *Adv. Mater.*, 2013, **25**, 2790–2796.
- 14 D. A. R. Barkhouse, R. Debnath, I. J. Kramer, D. Zhitomirsky, A. G. Pattantyus-Abraham, L. Levina, L. Etgar, M. Grätzel and E. H. Sargent, *Adv. Mater.*, 2011, **23**, 3134–3138.
- 15 A. K. Rath, M. Bernechea, L. Martinez, F. P. G. de Arquer, J. Osmond and G. Konstantatos, *Nat. Photonics*, 2012, **6**, 529–534.
- 16 A. K. Rath, F. Pelayo Garcia de Arquer, A. Stavrinadis, T. Lasanta, M. Bernechea, S. L. Diedenhofen and G. Konstantatos, *Adv. Mater.*, 2014, **26**, 4741–4747.
- 17 H. Wang, V. Gonzalez-Pedro, T. Kubo, F. Fabregat-Santiago, J. Bisquert, Y. Sanehira, J. Nakazaki and H. Segawa, *J. Phys. Chem. C*, 2015, **119**, 27265–27274.
- 18 P. R. Brown, R. R. Lunt, N. Zhao, T. P. Osedach, D. D. Wanger, L.-Y. Chang, M. G. Bawendi and V. Bulović, *Nano Lett.*, 2011, **11**, 2955–2961.
- 19 B. Ehrler, K. P. Musselman, M. L. Böhm, F. S. F. Morgenstern, Y. Vaynzof, B. J. Walker, J. L. MacManus-Driscoll and N. C. Greenham, *ACS Nano*, 2013, **7**, 4210–4220.
- 20 A. Stavrinadis, A. K. Rath, F. P. G. de Arquer, S. L. Diedenhofen, C. Magén, L. Martinez, D. So and G. Konstantatos, *Nat. Commun.*, 2013, **4**, 2981.
- 21 Z. Ning, O. Voznyy, J. Pan, S. Hoogland, V. Adinolfi, J. Xu, M. Li, A. R. Kirmani, J.-P. Sun, J. Minor, K. W. Kemp, H. Dong, L. Rollny, A. Labelle, G. Carey, B. Sutherland, I. Hill, A. Amassian, H. Liu, J. Tang, O. M. Bakr and E. H. Sargent, *Nat. Mater.*, 2014, **13**, 822–828.
- 22 O. Voznyy, D. Zhitomirsky, P. Stadler, Z. Ning, S. Hoogland and E. H. Sargent, *ACS Nano*, 2012, **6**, 8448–8455.
- 23 M. A. Green, K. Emery, Y. Hishikawa, W. Warta and E. D. Dunlop, *Prog. Photovoltaics Res. Appl.*, 2016, **24**, 3–11.
- 24 D. Scheunemann, S. Wilken, J. Parisi and H. Borchert, *Appl. Phys. Lett.*, 2013, **103**, 133902.
- 25 D. Scheunemann, S. Wilken, J. Parisi and H. Borchert, *ACS Photonics*, 2015, **2**, 864–875.
- 26 H. Borchert, D. Scheunemann, K. Frevert, F. Witt, A. Klein and J. Parisi, *Zeitschrift für Phys. Chemie*, 2015, **229**, 191–203.
- 27 M. G. Panthani, C. J. Stolle, D. K. Reid, D. J. Rhee, T. B. Harvey, V. A. Akhavan, Y. Yu and B. A. Korgel, *J. Phys. Chem. Lett.*, 2013, **4**, 2030–2034.
- 28 Q. Guo, G. M. Ford, H. W. Hillhouse and R. Agrawal, *Nano Lett.*, 2009, **9**, 3060–3065.
- 29 H. Azimi, T. Heumüller, A. Gerl, G. Matt, P. Kubis, M. Distaso, R. Ahmad, T. Akdas, M. Richter, W. Peukert and C. J. Brabec, *Adv. Energy Mater.*, 2013, **3**, 1589–1596.
- 30 J. E. Halpert, F. S. F. Morgenstern, B. Ehrler, Y. Vaynzof, D. Credgington and N. C. Greenham, *ACS Nano*, 2015, **9**, 5857–5867.
- 31 L. Li, N. Coates and D. Moses, *J. Am. Chem. Soc.*, 2010, **132**, 22–23.
- 32 H. McDaniel, N. Fuke, J. M. Pietryga and V. I. Klimov, *J. Phys. Chem. Lett.*, 2013, **4**, 355–361.
- 33 Z. Pan, I. Mora-Seró, Q. Shen, H. Zhang, Y. Li, K. Zhao, J. Wang, X. Zhong and J. Bisquert, *J. Am. Chem. Soc.*, 2014, **136**, 9203–9210.
- 34 D. H. Jara, S. J. Yoon, K. G. Stamplecoskie and P. V. Kamat, *Chem. Mater.*, 2014, **26**, 7221–7228.
- 35 J. Du, Z. Du, J.-S. Hu, Z. Pan, Q. Shen, J. Sun, D. Long, H. Dong, L. Sun, X. Zhong and L.-J. Wan, *J. Am. Chem. Soc.*, 2016, **138**, 4201–4209.
- 36 D. So and G. Konstantatos, *Chem. Mater.*, 2015, **27**, 8424–8432.
- 37 M. Nanu, J. Schoonman and A. Goossens, *Nano Lett.*, 2005, **5**, 1716–1719.
- 38 A. H. Cheshmekhavar, A. R. Mahjoub, H. Fakhri and M. Dehghani, *RSC Adv.*, 2015, **5**, 97381–97390.
- 39 Z. Chen, M. Tang, L. Song, G. Tang, B. Zhang, L. Zhang, J. Yang and J. Hu, *Nanoscale Res. Lett.*, 2013, **8**, 354.
- 40 D. Bozyigit, W. M. M. Lin, N. Yazdani, O. Yarema and V. Wood, *Nat. Commun.*, 2015, **6**, 6180.
- 41 J. Jasieniak, M. Califano and S. E. Watkins, *ACS Nano*, 2011, **5**, 5888–5902.
- 42 J. Sun, J. Zhao and Y. Masumoto, *Appl. Phys. Lett.*, 2013, **102**, 053119.
- 43 C. Krause, D. Scheunemann, J. Parisi and H. Borchert, *J. Appl. Phys.*, 2015, **118**, 205501.
- 44 T. Rath, M. Edler, W. Haas, A. Fischereeder, S. Moscher, A. Schenk, R. Trattnig, M. Sezen, G. Mauthner, A. Pein, D. Meischler, K. Bartl, R. Saf, N. Bansal, S. A. Haque, F. Hofer, E. J. W. List and G. Trimmel, *Adv. Energy Mater.*, 2011, **1**, 1046–1050.
- 45 S. B. Zhang, S.-H. Wei, A. Zunger and H. Katayama-Yoshida, *Phys. Rev. B*, 1998, **57**, 9642–9656.
- 46 S. Levchenko, N. N. Syrbu, V. E. Tezlevan, E. Arushanov, S. Doka-Yamigno, T. Schedel-Niedrig and M. C. Lux-Steiner, *J. Phys. Condens. Matter*, 2007, **19**, 456222.
- 47 D. A. R. Barkhouse, A. G. Pattantyus-Abraham, L. Levina and E. H. Sargent, *ACS Nano*, 2008, **2**, 2356–2362.
- 48 L. Lu, T. Zheng, Q. Wu, A. M. Schneider, D. Zhao and L. Yu, *Chem. Rev.*, 2015, **115**, 12666–12731.
- 49 D. Lee and K. Yong, *J. Phys. Chem. C*, 2014, **118**, 7788–7800.
- 50 Z. Sun, G. Sitbon, T. Pons, A. A. Bakulin and Z. Chen, *Sci. Rep.*, 2015, **5**, 10626.
- 51 Y. Yang, H. Zhong, Z. Bai, B. Zou, Y. Li, and G. D. Scholes, *J. Phys. Chem. C*, 2012, **116**, 7280.
- 52 A. Lefrançois, B. Luszczynska, B. Pepin-Donat, C. Lombard, B. Bouthinon, J.-M. Verilhac, M. Gromova, J. Faure-Vincent, S. Pouget, F. Chandezon, D. Sadki and P. Reiss, *Sci. Rep.* 2015, **5**, 7768.
- 53 R. Miranti, Y. Firdaus, E. Fron, M. Van der Auweraer, J. Parisi, and H. Borchert, *J. Phys. Chem. C*, 2015, **39** 22669–22680
- 54 C.-H. Chung, B. Bob, T.-B. Song and Y. Yang, *Sol. Energy Mater. Sol. Cells*, 2014, **120**, 642–646.
- 55 N. Zhao, T. P. Osedach, L.-Y. Chang, S. M. Geyer, D. Wanger, M. T. Binda, A. C. Arango, M. G. Bawendi and V. Bulovic, *ACS Nano*, 2010, **4**, 3743–3752.
- 56 C. J. Hages, N. J. Carter and R. Agrawal, *J. Appl. Phys.*, 2016, **119**, 014505.
- 57 M. Troviano and K. Taretto, *Sol. Energy Mater. Sol. Cells*, 2011, **95**, 3081–3086.
- 58 A. Foertig, J. Rauh, V. Dyakonov and C. Deibel, *Phys. Rev. B*, 2012, **86**, 115302.
- 59 T. Kirchartz, B. E. Pieters, J. Kirkpatrick, U. Rau and J. Nelson, *Phys. Rev. B*, 2011, **83**, 115209.
- 60 A. Shabaev, M. J. Mehl and A. L. Efros, *Phys. Rev. B*, 2015, **92**, 035431.
- 61 A. D. P. Leach and J. E. Macdonald, *J. Phys. Chem. Lett.*, 2016, **7**, 572–583.
- 62 K. E. Knowles, H. D. Nelson, T. B. Kilburn and D. R. Gamelin, *J. Am. Chem. Soc.*, 2015, **137**, 13138–13147.

Solid-State Colloidal CuInS₂ Quantum Dot Solar Cells enabled by Bulk Heterojunctions

David So, Santanu Pradhan and Gerasimos Konstantatos

Non-toxic colloidal quantum dot photovoltaics (CQD PV) are fabricated from CuInS₂ nanocrystals, expanding the materials systems used in CQD PV. Through control of device morphology, moving from a bilayer to a bulk heterojunction, the recombination from traps near the valence band is reduced.

TOC abstract figure

